FRONTIERS OF PHYSICS

RESEARCH ARTICLE
Volume 19 / Issue 3 / 33202 / 2024

Strong anisotropy of thermal transport in the monolayer of a new puckered phase of PdSe

Zheng Shu, Huifang Xu, Hejin Yan, Yongqing Cai†

Joint Key Laboratory of the Ministry of Education, Institute of Applied Physics and Materials Engineering, University of Macau, Taipa, Macau 999078, China
Corresponding author. E-mail: †yongqingcai@um.edu.mo
Received April 7, 2023; accepted October 6, 2023

ABSTRACT

We examine the electronic and transport properties of a new phase PdSe monolayer with a puckered structure calculated by first-principles and Boltzmann transport equation. The spin–orbit coupling is found to play a negligible effect on the electronic properties of PdSe monolayer. The lattice thermal conductivity of PdSe monolayer exhibits remarkable anisotropic characteristic due to anisotropic phonon group velocity along different directions and its intrinsic structure anisotropy. The compromised electronic mobility despite a relatively low thermal conduction results in a moderate *ZT* value but significantly anisotropic thermoelectric performance in single-layer PdSe. The present work suggests that the remarkable thermal transport anisotropy of PdSe monolayer can be used for thermal management, and enhance the scope of possibilities for heat flow manipulation in PdSe based devices. The sizeable puckered cages and wiggling lattice implies it an ideal platform for ionic and molecular engineering for thermoelectronic applications.

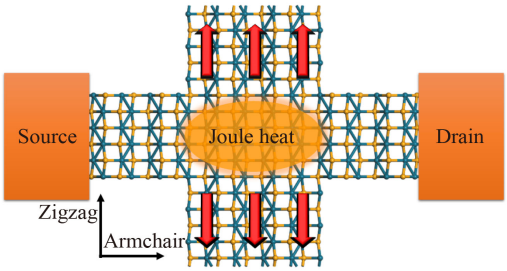

Keywords 2D materials, first-principles calculations, phonon

1 Introduction

Dimensionality reduction is an effective approach for discovering exotic materials with novel electronic and chemical properties [1–3]. Since the two-dimensional (2D) material graphene was exfoliated in 2004 [4], identifying similar layered systems has aroused much enthusiasm due to its intriguing properties, for example, ultrahigh electronic mobility and lattice thermal conductivity, which is significantly different from those of bulk graphite [5]. Subsequently, there are dozens of 2D materials being discovered that behaves in physical and chemical properties very differently compared to their 3D counterparts due to quantum confinement effect [6–10]. Ellis *et al.* [6] revealed that MoS_2 undergoes a transition from a direct to indirect gap semiconductor when a second layer is added to the monolayer MoS_2. Shu *et al.* [8] demonstrated that the diffusion rate of Li in γ-GeSe nanosheet is much faster than that in its bulk counterpart. Especially, 2D transition metal dichalcogenides (TMDs) have been widely used in electrocatalysis [11, 12], thermoelectrics [13], biosensor [14], and nanoelectronics [15].

Great efforts have also been devoted to exploring phase engineering of TMDs which possess versatile phases (i.e., 1H, 1T, 1T') with rich lattice, charge and orbital orderings [16]. $PdSe_2$ is one of the representatives of these 2D TMDs that exhibit the low-symmetry lattice, air stability, negative Poisson's ratio and high electrical conductivity [17–21]. Monolayer $PdSe_2$ is an indirect band gap semiconductor with a band gap of 1.30 eV and possesses a superior air stability [17, 18]. Liu *et al.* [19]

Higher Education Press

https://doi.org/10.1007/s11467-023-1354-7

showed that the negative Poisson's ratio can be observed in the $PdSe_2$ monolayer. Tangpakonsab *et al.* [21] unraveled the thermoelectric functionality of 2D penta-$PdSe_2$ with a maximized figure of merit ZT of 0.84 upon p-type doping at 900 K. Furthermore, the emission of Se atoms in layered $PdSe_2$ can result in the formation of the 2D new phase Pd_3Se_4 [22]. Xu *et al.* [23] proposed a guide for defect engineering of few-layer $PdSe_2$ and Pd_2Se_3 for functional devices. Naghavi *et al.* [24] suggests that Pd_3Se_4 monolayer possesses an ultralow lattice thermal conductivity and a high power factor as a promising thermoelectric material. Thus, it is of great importance to thoroughly study the properties of this type material by searching for new phase of 2D Pd–Se compound with different Pd:Se stoichiometry. Very recently, Huang *et al.* [25] predicted a hitherto unknown PdSe monolayer by particle swarm optimization (PSO) [26] method implemented in the Crystal structure Analysis by Particle Swarm Optimization (CALYPSO) [27] code. They revealed that PdSe possesses a better optical adsorption ability for visible light (VI) than those of Pd_2Se_4 and Pd_4Se_6 monolayers [25]. However, transport properties is an important physical quantities [28, 29], and the electrical and thermal transport properties of this new type PdSe monolayer is still unknown and needed to be explored.

Herein, for the first time, we investigated the electrical and thermal transport properties of a new phase of PdSe monolayer by using state-of-the-art density functional theory (DFT) combined with Boltzmann transport equation. We also discussed the anharmonic properties of PdSe monolayer through calculating Grüneisen parameter γ, the phonon group velocity v, phonon relaxation time τ and lattice thermal conductivity κ_l. Our results show that single-layer PdSe exhibits strong thermal transport anisotropy due to its intrinsic puckered structure and anisotropic phonon group velocity.

2 Computational methods

The first-principles calculations based on DFT theory are performed by using Vienna *ab initio* Simulation Package (VASP) [30, 31], choosing the projector-augmented wave (PAW) [32] pseudopotentials, and the generalized gradient approximation (GGA) of the Perdew–Burke–Ernzerhof [33] functional. The kinetic cut-off energy of plane wave and k-meshes for the crystal optimization are set to 400 eV and 6 × 11 × 1, respectively. The valence electron configurations employed for Pd and Se atoms are $3s^23p^64s^2$ and $4s^24p^65s^2$, respectively. The structure of PdSe is fully relaxed until the convergence criterions of the total energy and Hellmann–Feynman force are less than 1×10^{-8} eV and 0.001 eV·Å^{-1}, respectively. A vacuum layer of ~20 Å is built to avoid the interlayer interaction in the c-direction. A 3 × 4 × 1 supercell is adopted to test the thermal

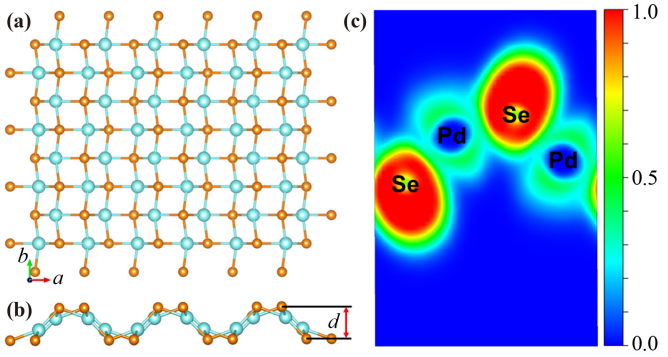

Fig. 1 **(a)** Top and **(b)** side views of the relaxed atomic structure of puckered PdSe monolayer. The unit cell is indicated by the black solid lines. **(c)** The electron localization function (ELF) of PdSe monolayer viewed along (010) direction. The blue and orange balls represent Pd and Se atoms, respectively.

stability of monolayer by *ab initio* molecular dynamics (AIMD) simulations. The canonical ensemble (NVT) with the Nosé–Hoover thermostat [34] is used in this work. The Heyd–Scuseria–Ernzerhof (HSE06) hybrid functional [35] is applied to calculate the band structure, and the result is compared with that of the PBE functional. The finite displacement method [36] is adopted to calculate the phonon dispersion and phonon density of states (pDOS) using a large 5 × 7 × 1 supercell. The rotational sum rules within the Born–Huang condition are considered to calibrate the second order force constants by Hiphive Package, which is proved to be important for obtaining the correct phonon dispersion of 2D materials [37].

The calculations of electrical transport properties are performed by the BoltzTraP2 code [38]. A dense k-mesh of 12 × 21 ×1 is adopted for the self-consistent calculation to obtain the reliable electrical transport results based on the HSE06 functional. The thermal transport properties are calculated using the ShengBTE code [39]. The second-order harmonic interatomic force constants (2nd IFCs) and third-order anharmonic IFCs (3rd IFCs) as the input files for ShengBTE are obtained by the finite displacement method. A cutoff distance of 10 nearest atomic neighbors with a 3 × 4 × 1 supercell is used for the calculation of 3rd IFC. The convergence tests of the Q-grids for the lattice thermal conductivity κ_l are carried out to ensure an enough sampling of the q-space of phonon for an accurate κ_l.

3 Results and discussion

The PdSe monolayer has a low-symmetry orthorhombic lattice structure, and the top and side views of its atomic structure are illustrated in Figs. 1(a) and (b). The lattice constants of PdSe monolayer are a = 8.13 Å

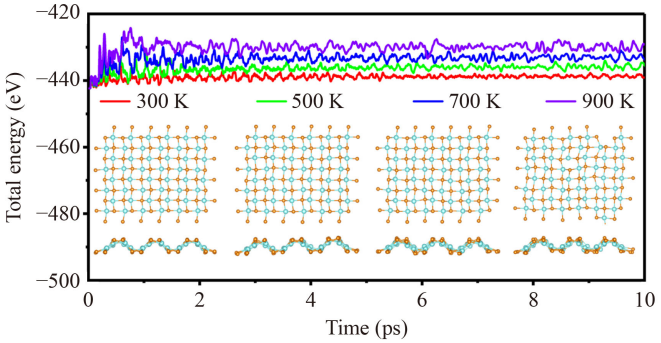

Fig. 2 Fluctuations of total energy during *ab initio* MD simulations for PdSe monolayer at T = 300, 500, 700 and 900 K with the annealing time of 10 ps.

and b = 4.67 Å under the GGA-PBE functional optimization without pressure, which is almost consistent with the previous report [25]. There is a wave-like structure connected by a Se–Pd–Pd–Se quartic-layer with Pd–Se–Pd bond angles of 70.57°, 89.99° and 113.59°. Intrinsically this highly anisotropic structure may lead to anisotropic transport properties along the orthogonal directions.

We firstly examine the electron localized function (ELF) which is able to measure the likelihood of finding another electron in the neighborhood space of an electron [40]. The values ranging from 0 to 1 reflect the bonding feature where high values close to ~1 represent a presence of strongly localized electrons. The calculated ELF of PdSe monolayer is shown in Fig. 1(c). We can observe that PdSe monolayer exhibits remarkable ionic bonding characteristics.

To study the thermal stability and examine the temperature dependent thermal transport of PdSe monolayer, the AIMD calculations are carried out with time step of 1 fs at 300, 500, 700 and 900 K. The snapshots after 10 ps simulations are shown in Fig. 2. During the 10 ps AIMD simulation, the energy oscillation of PdSe monolayer remains dynamic balance around a specific constant, even at 900 K. This implies that this structurally puckered PdSe can withstand temperatures as high as 900 K, implying this 2D phase has a superior thermal stability. Therefore, the temperature range 300–900 K is appropriate window for hosting thermal transport.

On the other hand, the electrical transport properties of materials highly depend on the electronic structure. For the orthorhombic system, the high symmetry points in the first Brillouin zone are Γ–X–S–Y–Γ, which is illustrated in Fig. 3(a). The calculated band structure of PdSe monolayer using GGA-PBE is presented in Fig. 3(b). We observe that the conduction band minimum (CBM) is located at the Γ–Y path, and the valence band maximum (VBM) is located at the Γ point under PBE level, showing an indirect band-gap semiconductor of 1.10 eV. Figure S1 of the Electronic Supplementary Materials (ESM) shows that the band edges are predominantly contributed by Pd 4d and Se 4p orbitals. However, Fig. 3(c) depicts the HSE06 electronic band structure and it exhibits the characteristics of direct bandgap semiconductors with a band gap of 1.40 eV. The CBM and VBM are both located at the Γ point under HSE06 level. In the calculations of transport properties, the shape of bands is more relevant, and the change of band gap is insignificant [41]. We have also examined the effect of spin–orbit coupling (SOC) on the band structure. The SOC has a crucial impact on the electronic properties for heavy elements. To clarify the influence of SOC on the electronic structures of the PdSe monolayer, we compared the band structure calculated with and without SOC based on the HSE06 functional. As shown in Fig. 3(d), the SOC correction slightly affects the band gap (1.39 eV) and band structure of PdSe. In view of this result, we next computed the electrical transport properties of PdSe monolayer by HSE06 functional without SOC.

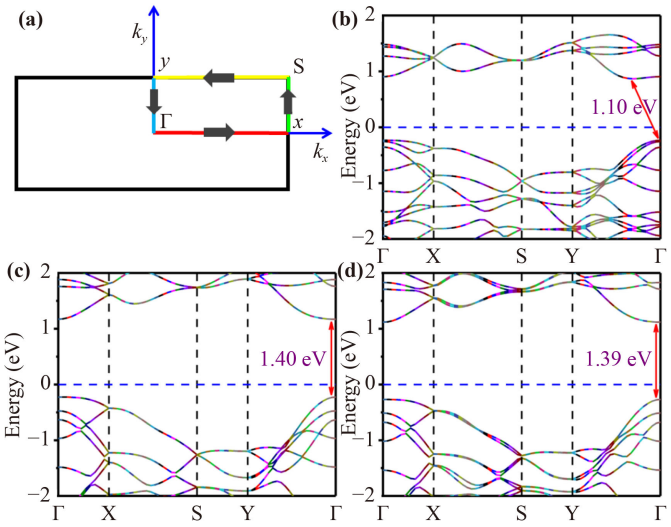

Fig. 3 **(a)** K-point path in the first Brillouin zone of PdSe. Band structures of PdSe monolayer calculated by **(b)** PBE, **(c)** HSE06 and **(d)** HSE06+SOC.

The conversion efficiency η of thermoelectric materials at the working temperature is generally determined by a dimensionless figure of merit: $ZT = S^2T\sigma/(\kappa_l + \kappa_e)$ [42, 43], where S, T, σ, κ_l and κ_e are the Seebeck coefficient, Kelvin temperature, electrical conductivity, lattice thermal conductivity and electronic thermal conductivity, respectively. Therefore, we firstly discuss the electrical transport properties of PdSe monolayer. Figures 4 and 5 show the electrical transport parameters for p- and n-type PdSe, respectively. Specially, the S of PdSe for p- and n-type doping at 300, 500, 700, and 900 K as a function of carrier concentration are shown in Fig. 4(a) and Fig. 5(a), respectively. As we can see, the S increases with the increasing T at the same carrier concentration, while it decreases with the increasing carrier concentration at the same T. Moreover, p-type doping PdSe exhibits a

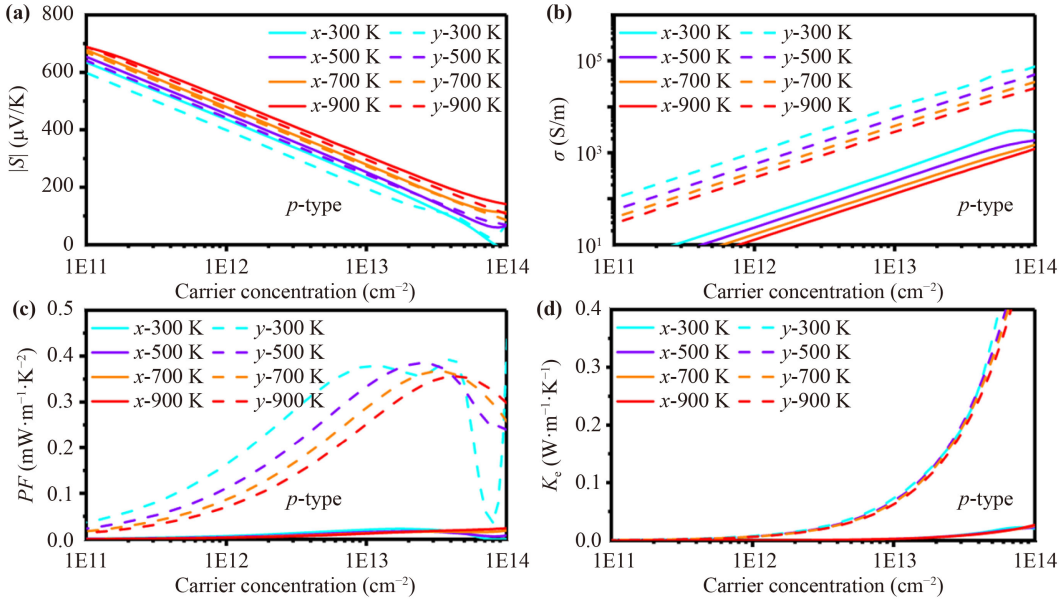

Fig. 4 Electronic transport properties of *p*-type PdSe monolayer. **(a)** Seebeck coefficient S, **(b)** electrical conductivity σ, **(c)** power factor σS^2 and **(d)** electronic thermal conductivity κ_e as a function of carrier concentration at temperature of 300, 500, 700 and 900 K.

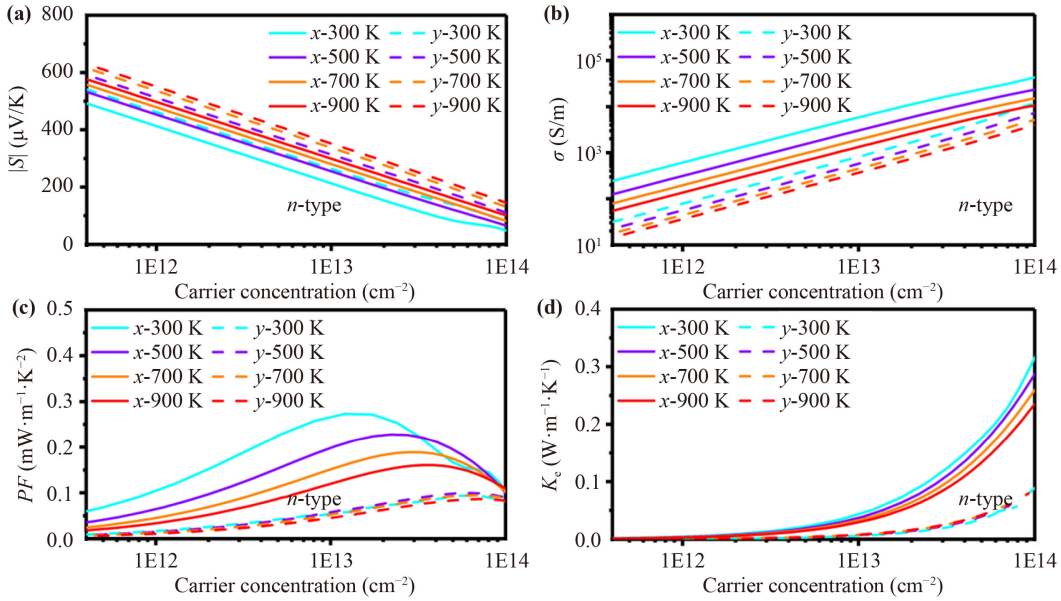

Fig. 5 Electronic transport properties of *n*-type PdSe monolayer. **(a)** Seebeck coefficient S, **(b)** electrical conductivity σ, **(c)** power factor σS^2 and **(d)** electronic thermal conductivity κ_e as a function of carrier concentration at temperature of 300, 500, 700 and 900 K.

larger S than *n*-type doping. Notably, the Seebeck coefficient for *p*-type doping at 300 K along the *x*-axis is ~630 μV/K at a concentration of 1.0×10^{11} cm^{-2}, exceeding those of phosphorene [44] and MoS_2 [45].

The electrical conductivity σ is another essential parameter for electrical transport. It can be obtained once we determine the carrier relaxation time τ using the deformation potential (DP) theory defined as [46]

$$\tau = \frac{\mu m^*}{e} = \frac{2\hbar^3 C_{2D}}{3k_B T m^* E_1^2}, \quad (1)$$

where $\hbar$, C_{2D}, k_B, m^* and E_1 are the Planck constant, elastic constant, Boltzmann constant, effective mass of electron or hole, and DP constant, respectively. The elastic constant can be calculated by the stress-strain relationship according to $C = [\partial^2 E/\partial(\Delta a/a_0)^2]/S_0$, where E, ε, k and E_{edge} are total energy of the system, the

Table 1 Results of the calculated deformation potential constants E_1, 2D elastic modulus C_{2D}, effective mass m^*, carrier mobility μ and relaxation time along the xx (a axis) and yy (b axis) directions of PdSe monolayer at 300 K.

Direction	Carrier type	E_1 (eV)	C_{2D} (J/m^2)	m^* (m_e)	μ (cm^2·V^{-1}·s^{-1})	τ ($\times$ 10^{-15} s)
xx (a axis)	Electron	2.36	13.57	2.97	3.91	6.61
	Hole	1.72	13.57	29.19	0.08	1.27
yy (b axis)	Electron	7.40	98.55	9.14	0.31	1.59
	Hole	9.70	98.55	1.82	4.48	4.64

band energy, the electron wave vector and the energy of band edge under the bi-axial strain (–1.5%, –1%, –0.5%, 0, 0.5%, 1% and 1.5% as sampling points), S_0 is the area of an 2D material, and $\Delta a/a_0$ is the change ratio of lattice constant compared to the equilibrium state, respectively. Additionally, the DP constant is described as $C = \partial E_{edge}/\partial(\Delta a/a_0)$, where E_{edge} is CBM or VBM. The calculated deformation potential constant E_1, elastic moduli C_{2D}, and carrier effective mass m^* are compiled in Table 1. The E_1 of electrons (holes) along the x-axis and y-axis are 2.36 (1.72) and 7.40 (9.70) eV, respectively. Moreover, the C_{2D} is estimated to be 13.57 (98.55) J/m^2 along the x-axis (y-axis). The difference of C_{2D} demonstrates that PdSe monolayer is softer along the x-axis. Based on all factors obtained from DFT calculations, the electrical conductivity σ, power factor σS^2, and electronic thermal conductivity of PdSe monolayer at 300, 500, 700, and 900 K as a function of carrier concentration under hole and electron doping are shown in Figs. 4(b)–(d) and Figs. 5(b)–(d), respectively. The electrical conductivity σ shows the opposite behavior compared to Seebeck coefficient S due to the reciprocal relationship between them. Figures 4(c) and 5(c) show that PF therefore is not monotonically related to the carrier concentration because a higher carrier concentration enhances σ and κ_e but reduces S. The maximum PFs at 900 K of PdSe monolayer for p- and n-type doping are 0.36 mW·m^{-1}·K^{-2} along y-axis and 0.16 mW·m^{-1}·K^{-2} along x-axis, respectively. Moreover, the flat band edges of PdSe monolayer result in a low carrier mobility and a short relaxation time, especially for the hole along the x-axis. Therefore, the σ, PF and κ_e of PdSe monolayer are relatively low. These results imply that the thermal transport of PdSe monolayer is largely dominated by phonons because of its relatively low electrical conductivity and carrier mobility. It is worth noting that the DP theory only consider scattering from the longitudinal phonons while neglecting the scatterings from other types of phonons. A more accurate estimation of the relaxation time requires solving the electron-phonon coupling (EPC) [43]. Unfortunately, the EPC method is extremely computational-consuming for complex materials (the primitive cell of PdSe contains 8 atoms). In addition, the carrier relaxation time of single-layer PdSe is quite short due to the large m^* caused by the flat band edge, so the EPC method cannot change the fact of the low σ and PF.

Concerning the lattice dynamics, from the phonon spectrum in Fig. S2(a) of the ESM, we can see that there are 24 phonon branches, including 3 acoustic phonon branches and 21 optical phonon branches. The three branches originating from the Γ-point are acoustic modes, namely the out-of-plane acoustic (ZA) mode, the transversal acoustic (TA) mode and the longitudinal acoustic (LA) mode, which are labeled by green, red and blue colors, respectively. The highest vibration frequency of PdSe monolayer is 7.34 THz, which is higher than that of α-GeSe [47], and lower than those of β-GeSe [47] and γ-GeSe [43, 47]. Furthermore, there is no imaginary-frequency in the first Brillouin zone, suggesting the dynamical stability of PdSe monolayer in accordance with Huang *et al.* [25]. There is a crossover phenomenon between the high-frequency acoustic branch LA mode and the low-frequency optical branches in the X–Y path. In addition, a similar phenomenon can also be observed between ZA and TA modes. This result suggests that strong coupling may exist in these modes, which can lead to a low κ_l [48, 49]. Obviously, the phonon dispersion shows a high anisotropy in the x- and y-axis, resulting in high anisotropy of phonon group velocities in different directions. Furthermore, the distribution of pDOS of PdSe is plotted in Fig. S2(b) of the ESM. Analysis of the pDOS indicates that the phonon branches in the frequency of 0–3.09 THz are mainly contributed by Pd atoms while the phonon branches in the frequency of 4.60–6.54 THz are dominated by Se atoms.

Subsequently, we show the lattice thermal conductivity κ_l of PdSe as a function of temperature in Fig. 6(a). It should be noted that κ_l is corrected by a factor of h/d_0, where h is the thickness in the z-axis and d_0 is the effective thickness. The effective thickness is defined as the summation of the buckling height and the van der Waals radii of two outmost atoms [39]. As we can see, the κ_l reduces with the rising temperatures along the x- and y-axis, following a T^{-1} dependence. The κ_l along x-axis (10.55 W·m^{-1}·K^{-1} at 300 K and 3.47 W·m^{-1}·K^{-1} at 900 K) is ~3 times larger than that of y-axis (3.60 W·m^{-1}·K^{-1} at 300 K and 1.21 W·m^{-1}·K^{-1} at 900 K). This highly in-plane anisotropic κ_l of PdSe monolayer originates from its unique "puckered" structure. At T = 300 K, the κ_l of PdSe in the x-axis is higher than those of SnSe along the zigzag direction (2.95 W·m^{-1}·K^{-1}) [50], γ-GeS (1.07 W·m^{-1}·K^{-1}) [43] and MoO_3 along x direction (1.57 W·m^{-1}·K^{-1}) [51], close to those of penta-$PdSe_2$

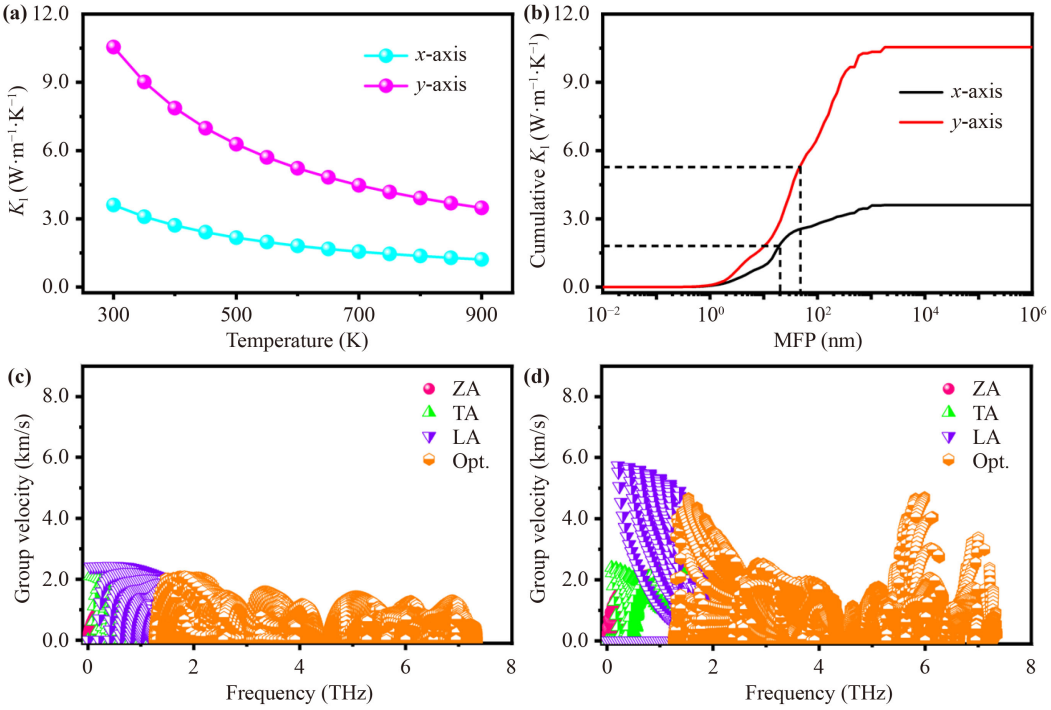

Fig. 6 **(a)** The temperature dependent lattice thermal conductivity κ_l. **(b)** The cumulative thermal conductivity of PdSe. The phonon group velocity along the **(c)** x-axis and **(d)** y-axis.

along the x-direction (3.60 W·m^{-1}·K^{-1}) [19], Janus γ-GeSSe (3.33 W·m^{-1}·K^{-1}) [52], ZrS_2 (3.29 W·m^{-1}·K^{-1}) [53] and γ-GeSe (3.39 W·m^{-1}·K^{-1}) [43], and smaller than those of α-GeSe along the armchair direction (4.57 W·m^{-1}·K^{-1}) [50] and 1T′ $MoTe_2$ in the y direction (13.02 W·m^{-1}·K^{-1}) [54]. In addition, the cumulative thermal conductivity with respect to the phonon maximum mean-free path (MFP) is also calculated to analyze the size dependence of κ_l [51, 54], which is plotted in Fig. 6(b). Furthermore, phonons with MFPs about 20 (48) nm contribute 50% of the total κ_l along the x-axis (y-axis), reflects the characteristic length of the nanostructured PdSe and implies a stronger quantum confinement effect along the x-axis direction.

The thermal conductivity can be written as a summation of all phonon modes, which can be described as

$$\kappa_{l,\alpha\beta} = \frac{1}{N_q}\sum\nolimits_{\lambda} c_{\lambda} v_{\lambda,\alpha} v_{\lambda,\beta} \tau_{\lambda}. \quad (2)$$

Here, N_q is the total number of sampling q-points in the first Brillouin zone, whereas c_λ, $v_{\lambda,\alpha}$ ($v_{\lambda,\beta}$) and τ_λ are the volumetric heat capacity, phonon group velocity along the α-direction (β-direction), and phonon relaxation time of the phonon mode λ. The phonon group velocity of PdSe is shown in Figs. 6(c) and (d), and the values along the x-axis are significantly smaller than those along the y-axis in total. The origin of anisotropic κ_l is attributed to the strong anisotropic phonon group velocity towards different directions. Such anisotropic thermal conduction is desired for heat management [55]. Phonon anharmonicity makes the dominant contribution for the lattice thermal conductivity [56]. To further quantify the anharmonic properties that lead to ultralow κ_l of PdSe monolayer, the mode distribution of Grüneisen parameter γ is shown in Fig. S4(a) of the ESM. This physical quantity is defined as $\gamma_\lambda = -\frac{A}{\omega_\lambda}\frac{\partial \omega_\lambda}{\partial A}$, where A is the area of the 2D unit cell and ω_λ is the angular frequency of a specific phonon mode λ. A large γ implies large anharmonicity. We can observe a giant anharmonicity of ZA mode. What's more, Fig. S4(b) of the ESM shows the phonon lifetime of PdSe, which mainly lies in the range of 0.1 and 100 ps. We find that the phonon lifetime of ZA mode is comparable to those of TA and LA modes, suggesting a strong in-plane and out-of-plane mode coupling.

Figure 7 demonstrates the ZT values of n- and p-type single-layer PdSe at different temperatures as a function of carrier concentration along the x- and y-axis. Interestingly, the ZT value for p-type doping along the y-axis is much larger than that along the x-axis, while the ZT value for n-type doping along the x-axis is much larger than that along the y-axis. Thus, the ZT value of each carrier type shows a significant parity difference and a remarkable direction-dependent anisotropy. The maximum ZT value of the p-type (n-type) PdSe monolayer along y-axis (x-axis) increases from 0.016 (0.022) at 300 K to 0.086 (0.111) at 900 K. Consequently, even though PdSe has a high S and low κ_l, it exhibits moderate maximum values of ZT due to large m^* associated with the flat band edge and the low σ.

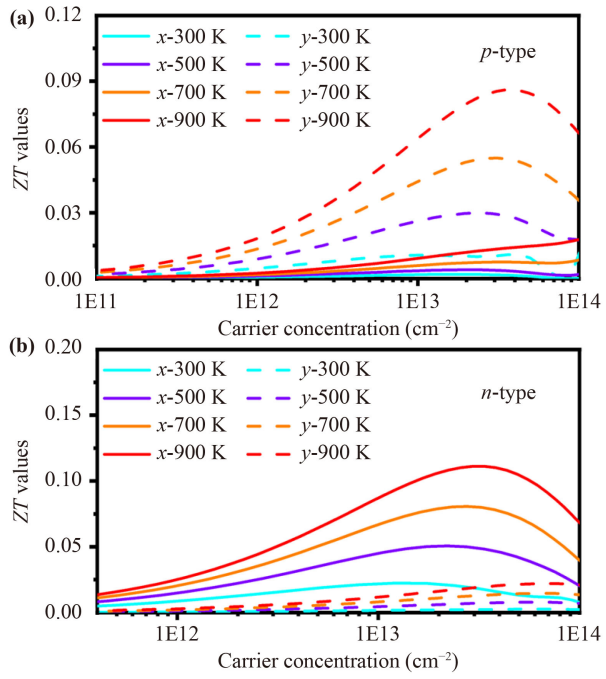

Fig. 7 The ZT values for **(a)** p- and **(b)** n-type PdSe monolayer as a function of carrier concentration at temperature of 300, 500, 700 and 900 K.

4 Conclusions

In summary, we have investigated the electronic structure and transport properties of a new phase single-layer PdSe through DFT calculations with the Boltzmann transport equation. Our results show that the single-layer PdSe exhibits a strong anisotropy of electronic structures and a direct band gap of 1.40 eV under the HSE06 functional level. Intriguingly, the single-layer PdSe also exhibits highly thermal transport anisotropy: thermal conductivity in the y-axis is ~3 times larger than that in the x-axis. This can be attributed to its intrinsic puckered structure and anisotropic phonon group velocity. Our work reveals the anisotropic physics of PdSe monolayer and such properties can enable heat flow manipulation in PdSe-based devices to improve thermal management. In addition, despite a limited performance of the ZT value of the intrinsic PdSe, its sizeable puckered cages and a unique wiggling lattice suggests that it would an ideal host for ionic doping and molecular decoration for improving electronic conductivity and thus a promising thermoelectronic application.

Declarations The authors declare that they have no competing interests and there are no conflicts.

Electronic supplementary materials The online version contains supplementary material available at https://doi.org/10.1007/s11467-023-1354-7 and https://journal.hep.com.cn/fop/EN/10.1007/s11467-023-1354-7.

Acknowledgements This work was supported by the National Natural Science Foundation of China (Grant No. 22022309) and the Natural Science Foundation of Guangdong Province, China (No. 2021A1515010024), the University of Macau (Nos. SRG2019-00179-IAPME and MYRG2020-00075-IAPME), and the Science and Technology Development Fund from Macau SAR (No. FDCT-0163/2019/A3). This work was performed in part at the High-Performance Computing Cluster (HPCC) which is supported by Information and Communication Technology Office (ICTO) of the University of Macau.

References

1. K. S. Novoselov, V. I. Fal′ko, L. Colombo, P. R. Gellert, M. G. Schwab, and K. Kim, A roadmap for graphene, *Nature* 490(7419), 192 (2012)
2. G. Shan, Z. Ding, and Y. Gogotsi, Two-dimensional MXenes and their applications, *Front. Phys.* 18(1), 13604 (2023)
3. K. S. Novoselov, D. V. Andreeva, W. C. Ren, and G. C. Shan, Graphene and other two-dimensional materials, *Front. Phys.* 14(1), 13301 (2019)
4. K. S. Novoselov, A. K. Geim, S. V. Morozov, D. Jiang, Y. Zhang, S. V. Dubonos, I. V. Grigorieva, and A. A. Firsov, Electric field effect in atomically thin carbon films, *Science* 306(5696), 666 (2004)
5. W. Cai, A. L. Moore, Y. Zhu, X. Li, S. Chen, L. Shi, and R. S. Ruoff, Thermal transport in suspended and supported monolayer graphene grown by chemical vapor deposition, *Nano Lett.* 10(5), 1645 (2010)
6. J. K. Ellis, M. J. Lucero, and G. E. Scuseria, The indirect to direct band gap transition in multilayered MoS_2 as predicted by screened hybrid density functional theory, *Appl. Phys. Lett.* 99(26), 261908 (2011)
7. H. Li, Q. Zhang, C. C. R. Yap, B. K. Tay, T. H. T. Edwin, A. Olivier, and D. Baillargeat, From bulk to monolayer MoS_2: Evolution of Raman scattering, *Adv. Funct. Mater.* 22(7), 1385 (2012)
8. Z. Shu, X. Cui, B. Wang, H. Yan, and Y. Cai, Fast intercalation of lithium in semi-metallic γ-GeSe nanosheet: A new group-IV monochalcogenide for lithium-ion battery application, *ChemSusChem* 15(15), e202200564 (2022)
9. Y. Feng, W. Zhou, Y. Wang, J. Zhou, E. Liu, Y. Fu, Z. Ni, X. Wu, H. Yuan, F. Miao, B. Wang, X. Wan, and D. Xing, Raman vibrational spectra of bulk to monolayer ReS_2 with lower symmetry, *Phys. Rev. B* 92(5), 054110 (2015)
10. A. Laturia, M. L. Van de Put, and W. G. Vandenberghe, Dielectric properties of hexagonal boron nitride and transition metal dichalcogenides: From monolayer to bulk, *npj 2D Mater. Appl.* 2(1), 6 (2018)
11. T. Yang, T. T. Song, J. Zhou, S. Wang, D. Chi, L. Shen, M. Yang, and Y. P. Feng, High-throughput screening of transition metal single atom catalysts anchored on molybdenum disulfide for nitrogen fixation, *Nano Energy* 68, 104304 (2020)
12. Z. Shu, H. Yan, H. Chen, and Y. Cai, Mutual modulation via charge transfer and unpaired electrons of catalytic sites for the superior intrinsic activity of N_2 reduction:

From high-throughput computation assisted with a machine learning perspective, *J. Mater. Chem. A* 10(10), 5470 (2022)
13. L. Pan, Z. Wang, J. Carrete, and G. K. H. Madsen, Thermoelectric properties of the Janus PtSTe monolayer compared with its parent structures, *Phys. Rev. Mater.* 6(8), 084005 (2022)
14. C. Tan, P. Yu, Y. Hu, J. Chen, Y. Huang, Y. Cai, Z. Luo, B. Li, Q. Lu, L. Wang, Z. Liu, and H. Zhang, High-yield exfoliation of ultrathin two-dimensional ternary chalcogenide nanosheets for highly sensitive and selective fluorescence DNA sensors, *J. Am. Chem. Soc.* 137(32), 10430 (2015)
15. E. Liu, Y. Fu, Y. Wang, Y. Feng, H. Liu, X. Wan, W. Zhou, B. Wang, L. Shao, C. H. Ho, Y. S. Huang, Z. Cao, L. Wang, A. Li, J. Zeng, F. Song, X. Wang, Y. Shi, H. Yuan, H. Y. Hwang, Y. Cui, F. Miao, and D. Xing, Integrated digital inverters based on two-dimensional anisotropic ReS_2 field-effect transistors, *Nat. Commun.* 6(1), 6991 (2015)
16. J. Yuan, Y. Chen, Y. Xie, X. Zhang, D. Rao, Y. Guo, X. Yan, Y. P. Feng, and Y. Cai, Squeezed metallic droplet with tunable Kubo gap and charge injection in transition metal dichalcogenides, *Proc. Natl. Acad. Sci. USA* 117(12), 6362 (2020)
17. A. D. Oyedele, S. Yang, L. Liang, A. A. Puretzky, K. Wang, J. Zhang, P. Yu, P. R. Pudasaini, A. W. Ghosh, Z. Liu, C. M. Rouleau, B. G. Sumpter, M. F. Chisholm, W. Zhou, P. D. Rack, D. B. Geohegan, and K. Xiao, $PdSe_2$: Pentagonal two-dimensional layers with high air stability for electronics, *J. Am. Chem. Soc.* 139(40), 14090 (2017)
18. A. N. Hoffman, Y. Gu, L. Liang, J. D. Fowlkes, K. Xiao, and P. D. Rack, Exploring the air stability of $PdSe_2$ via electrical transport measurements and defect calculations, *npj 2D Mater. Appl.* 3(1), 50 (2019)
19. G. Liu, Q. Zeng, P. Zhu, R. Quhe, and P. Lu, Negative Poisson's ratio in monolayer $PdSe_2$, *Comput. Mater. Sci.* 160, 309 (2019)
20. A. V. Kuklin and H. Ågren, Quasiparticle electronic structure and optical spectra of single-layer and bilayer $PdSe_2$: Proximity and defect-induced band gap renormalization, *Phys. Rev. B* 99(24), 245114 (2019)
21. P. Tangpakonsab, P. Moontragoon, T. Hussain, and T. Kaewmaraya, Thermoelectric efficiency of two-dimensional pentagonal-$PdSe_2$ at high temperatures and the role of strain, *ACS Appl. Energy Mater.* 5(11), 14522 (2022)
22. J. Lin, S. Zuluaga, P. Yu, Z. Liu, S. T. Pantelides, and K. Suenaga, Novel Pd_2Se_3 two-dimensional phase driven by interlayer fusion in layered $PdSe_2$, *Phys. Rev. Lett.* 119(1), 016101 (2017)
23. X. Xu, J. Robertson, and H. Li, Semiconducting few-layer $PdSe_2$ and Pd_2Se_3: Native point defects and contacts with native metallic $Pd_{17}Se_{15}$, *Phys. Chem. Chem. Phys.* 22(14), 7365 (2020)
24. S. S. Naghavi, J. He, Y. Xia, and C. Wolverton, Pd_2Se_3 monolayer: A promising two-dimensional thermoelectric material with ultralow lattice thermal conductivity and high power factor, *Chem. Mater.* 30(16), 5639 (2018)
25. M. Huang, X. Jiang, Y. Zheng, Z. Xu, X. X. Xue, K. Chen, and Y. Feng, Novel two-dimensional PdSe phase: A puckered material with excellent electronic and optical properties, *Front. Phys.* 17(5), 53504 (2022)
26. S. T. Call, D. Y. Zubarev, and A. I. Boldyrev, Global minimum structure searches via particle swarm optimization, *J. Comput. Chem.* 28(7), 1177 (2007)
27. Y. Wang, J. Lv, L. Zhu, and Y. Ma, CALYPSO: A method for crystal structure prediction, *Comput. Phys. Commun.* 183(10), 2063 (2012)
28. L. Chen, K. Li, X. Peng, H. Lian, X. Lin, and Z. Fu, Isogeometric boundary element analysis for 2D transient heat conduction problem with radial integration method, *Comput. Model. Eng. Sci.* 126(1), 125 (2021)
29. H. Cheng, Z. Xing, and M. Peng, The improved element-free Galerkin method for anisotropic steady-state heat conduction problems, *Comput. Model. Eng. Sci.* 132(3), 945 (2022)
30. G. Kresse and J. Furthmüller, Efficiency of *ab-initio* total energy calculations for metals and semiconductors using a plane-wave basis set, *Comput. Mater. Sci.* 6(1), 15 (1996)
31. G. Kresse and J. Furthmüller, Efficient iterative schemes for *ab initio* total-energy calculations using a plane-wave basis set, *Phys. Rev. B* 54(16), 11169 (1996)
32. P. E. Blöchl, Projector augmented-wave method, *Phys. Rev. B* 50(24), 17953 (1994)
33. J. P. Perdew, K. Burke, and M. Ernzerhof, Generalized gradient approximation made simple, *Phys. Rev. Lett.* 77(18), 3865 (1996)
34. G. J. Martyna, M. L. Klein, and M. Tuckerman, Nosé–Hoover chains: The canonical ensemble via continuous dynamics, *J. Chem. Phys.* 97(4), 2635 (1992)
35. J. Heyd, G. E. Scuseria, and M. Ernzerhof, Hybrid functionals based on a screened Coulomb potential, *J. Chem. Phys.* 118(18), 8207 (2003)
36. A. Togo, F. Oba, and I. Tanaka, First-principles calculations of the ferroelastic transition between rutile-type and $CaCl_2$-type SiO_2 at high pressures, *Phys. Rev. B* 78(13), 134106 (2008)
37. F. Eriksson, E. Fransson, and P. Erhart, The Hiphive Package for the extraction of high-order force constants by machine learning, *Adv. Theory Simul.* 2(5), 1800184 (2019)
38. G. K. H. Madsen, J. Carrete, and M. J. Verstraete, BoltzTraP2, a program for interpolating band structures and calculating semi-classical transport coefficients, *Comput. Phys. Commun.* 231, 140 (2018)
39. W. Li, J. Carrete, N. A. Katcho, and N. Mingo, ShengBTE: A solver of the Boltzmann transport equation for phonons, *Comput. Phys. Commun.* 185(6), 1747 (2014)
40. A. D. Becke and K. E. Edgecombe, A simple measure of electron localization in atomic and molecular systems, *J. Chem. Phys.* 92(9), 5397 (1990)
41. J. Ma, F. Meng, J. He, Y. Jia, and W. Li, Strain-induced ultrahigh electron mobility and thermoelectric figure of merit in monolayer α-Te, *ACS Appl. Mater. Interfaces* 12(39), 43901 (2020)
42. L. D. Zhao, S. H. Lo, Y. Zhang, H. Sun, G. Tan, C. Uher, C. Wolverton, V. P. Dravid, and M. G. Kanatzidis, Ultralow thermal conductivity and high thermoelectric figure of merit in SnSe crystals, *Nature*

508(7496), 373 (2014)
43. Z. Shu, B. Wang, X. Cui, X. Yan, H. Yan, H. Jia, and Y. Cai, High-performance thermoelectric monolayer γ-GeSe and its group-IV monochalcogenide isostructural family, *Chem. Eng. J.* 454, 140242 (2023)
44. H. Y. Lv, W. J. Lu, D. F. Shao, and Y. P. Sun, Enhanced thermoelectric performance of phosphorene by strain-induced band convergence, *Phys. Rev. B* 90(8), 085433 (2014)
45. W. Y. Lee, M. S. Kang, N. W. Park, G. S. Kim, A. D. Nguyen, J. W. Choi, Y. G. Yoon, Y. S. Kim, H. W. Jang, E. Saitoh, and S. K. Lee, Layer dependence of out-of-plane electrical conductivity and Seebeck coefficient in continuous mono-to multilayer MoS_2 films, *J. Mater. Chem. A* 9(47), 26896 (2021)
46. J. Bardeen and W. Shockley, Deformation potentials and mobilities in non-polar crystals, *Phys. Rev.* 80(1), 72 (1950)
47. B. Wang, X. Yan, X. Cui, and Y. Cai, First-principles study of the phonon lifetime and low lattice thermal conductivity of monolayer γ-GeSe: A comparative study, *ACS Appl. Nano Mater.* 5(10), 15441 (2022)
48. N. Wang, M. Li, H. Xiao, X. Zu, and L. Qiao, Layered LaCuOSe: A promising anisotropic thermoelectric material, *Phys. Rev. Appl.* 13(2), 024038 (2020)
49. G. Zhang and Y. W. Zhang, Thermoelectric properties of two-dimensional transition metal dichalcogenides, *J. Mater. Chem. C* 5(31), 7684 (2017)
50. G. Qin, Z. Qin, W. Z. Fang, L. C. Zhang, S. Y. Yue, Q. B. Yan, M. Hu, and G. Su, Diverse anisotropy of phonon transport in two-dimensional group IV–VI compounds: A comparative study, *Nanoscale* 8(21), 11306 (2016)
51. Z. Tong, T. Dumitrică, and T. Frauenheim, Ultralow thermal conductivity in two-dimensional MoO_3, *Nano Lett.* 21(10), 4351 (2021)
52. V. V. Thanh, D. V. Truong, and N. T. Hung, Janus γ-GeSSe monolayer as a high-performance material for photocatalysis and thermoelectricity, *ACS Appl. Energy Mater.* 6(2), 910 (2023)
53. H. Y. Lv, W. J. Lu, D. F. Shao, H. Y. Lu, and Y. P. Sun, Strain-induced enhancement in the thermoelectric performance of a ZrS_2 monolayer, *J. Mater. Chem. C* 4(20), 4538 (2016)
54. X. Cui, X. Yan, B. Wang, and Y. Cai, Phononic transport in 1T′-$MoTe_2$: Anisotropic structure with an isotropic lattice thermal conductivity, *Appl. Surf. Sci.* 608, 155238 (2023)
55. Y. Su, C. Deng, J. Liu, X. Zheng, Y. Wei, Y. Chen, W. Yu, X. Guo, W. Cai, G. Peng, H. Huang, and X. Zhang, Highly in-plane anisotropy of thermal transport in suspended ternary chalcogenide Ta_2NiS_5, *Nano Res.* 15(7), 6601 (2022)
56. X. Yan, B. Wang, Y. Hai, D. R. Kripalani, Q. Ke, and Y. Cai, Phonon anharmonicity and thermal conductivity of two-dimensional van der Waals materials: A review, *Sci. China Phys. Mech. Astron.* 65(11), 117004 (2022)